arXiv:2008.12924v1 [physics.flu-dyn] 29 Aug 2020

Towards human-interpretable, automated learning of feedback control for the mixing layer

Hao Li[1,2]**, Guy Y. Cornejo Maceda**[3]**, Yiqing Li**[4]**, Jianguo Tan**[1†]**,**
Marek Morzyński[5] **and Bernd R. Noack**[4,2]**†**

[1] Scicence and Technology on Scramjet Laboratory,
National University of Defense Technology, Changsha, Hunan Province, China

[2] Hermann-Föttinger-Institut, Technische Universität Berlin,
Müller-Breslau-Straße 8, D-10623 Berlin, Germany

[3] LIMSI, CNRS, Université Paris-Saclay, Bât 507, rue du Belvédère, Campus Universitaire, F-91403
Orsay, France

[4] Center for Turbulence Control, Harbin Institute of Technology, Shenzhen, Room 312, Building C,
University Town, Xili, Shenzhen 518058, China

[5] Chair of Virtual Engineering, Poznań University of Technology,
Jana Pawła II 24 street, 60-965 Poznań, Poland

We propose an automated analysis of the flow control behaviour from an ensemble of control laws and associated time-resolved flow snapshots. The input may be the rich data base of machine learning control (MLC) optimizing a feedback law for a cost function in the plant. The proposed methodology provides (1) insights into control landscape which maps control laws to performance including extrema and ridge-lines, (2) a catalogue of representative flow states and their contribution to cost function for investigated control laws and (3) a visualization of the dynamics. Key enablers are classification and feature extraction methods of machine learning. The analysis is successfully applied to the stabilization of a mixing layer with sensor-based feedback driving an upstream actuator. The fluctuation energy is reduced by 26%. The control replaces unforced Kelvin-Helmholtz vortices with subsequent vortex pairing by higher-frequency Kelvin-Helmholtz structures of lower energy. These efforts target a human interpretable, fully automated analysis of MLC identifying qualitatively different actuation regimes, distilling corresponding coherent structures, and developing a digital twin of the plant.

1. Introduction

We augment an automated learning of flow control by an analysis which may provide physical insights into qualitatively different regimes and the coherent structure dynamics. The vast majority of active turbulence control studies are performed in a model-free manner (Brunton & Noack 2015), as control-oriented modeling of the actuation response from broadband frequency dynamics is still a challenge.

Steady or periodic operation of a single actuator may be optimized by gradient-based approaches for one or few parameters, like extremum seeking. However, the optimization of multiple actuators, feedback with multiple sensors, or more complex control dynamics naturally gives rise to rich search space of control laws. The underlying regression problem aims to optimize a cost function for a multiple-input multiple-output control law. Machine learning provides powerful regression solvers for complex optimization problems (Fukami *et al.* 2020). Evolutionary algorithms (Koumoutsakos *et al.* 2001), genetic algorithms (Benard *et al.* 2016),

† Email address for correspondence: jianguotan@nudt.edu.cn, bernd.noack@hit.edu.cn

genetic programming (Li *et al.* 2018), cluster-based control (Nair *et al.* 2019), and reinforcement learning (Rabault *et al.* 2019) may serve as examples. Most optimizations require dozens to thousands of statistically representative performance tests of control laws. Typically, the best control law and few associated flow fields are present while the vast majority of the created data base is ignored. This study aims to use this data base for physically interpreting the learning process. Starting point is the metric of attractor overlap (Ishar *et al.* 2019).

This study focuses on sensor-based stabilization of the mixing layer as notoriously difficult and well investigated control benchmark. The mixing layer plays an important role for drag reduction, separation mitigation, combustion enhancement, noise reduction, to name only a few configurations. Open-loop investigations indicate that carefully calibrated multi-frequency actuation may significantly enhance mixing increase (Coats 1997) while high-frequency actuation stabilizes the mixing layer over a limited streamwise extent. Curiously, a low-frequency actuation with about 63% of the natural shedding frequency is found to have a stabilizing effect on shear layers (Pastoor *et al.* 2008). The literature on in-time feedback control is sparse (Wiltse & Glezer 2011). Phasor control may strongly destabilize the flow (Parezanović *et al.* 2016). The direct stabilization may be achieved by opposition control, i.e., when actuation and sensors are at the same location. But it is notoriously difficult if sensors are several wavelengths downstream of the actuation, as the mixing layer has a continuum of unstable frequencies. The present study is based on a direct numerical simulation for the two-dimensional mixing layer with upstream actuation and a downstream array of sensors. The actuation leads to dynamically rich behaviour while remaining computationally doable and physically interpretable. The optimization is performed with linear genetic programming control (Li *et al.* 2018). The employed optimizer has cracked the most challenging control problems in the past but this choice not essential for the proposed analysis methods.

In this paper, we aim to augment machine learning control as automated and human-intepretable learning of feedback control exploiting the complete data base of simulations. The paper is organized as follows. § 2 describes the numerical simulation and control of the mixing layer. § 3 describes the MLC system and the analysis methods. In § 4, the MLC for mixing destabilization and stabilization is analyzed. Finally, conclusions and outlook are provided in § 5.

2. Mixing layer plant—Configuration and control problem

In the present study, an incompressible two-dimensional mixing layer with the velocity ratio 3 : 1 is considered as the control plant. The flow is actuated by a small upstream volume force in the center of the mixing layer and is monitored by a two-dimensional array of 5×5 downstream velocity sensors. The cost to be optimized is the cumulative fluctuation energy of these sensors.

The location vector is denoted by $\boldsymbol{x} = (x, y)$ where the x-axis is aligned with the streamwise direction and the y-axis denotes the transverse direction. The origin of the coordinate system is located at the left edge of actuation zone. The velocity field is represented by $\boldsymbol{u} = (u, v)$ where u and v are the streamwise and transverse component, respectively. All variables are assumed to be non-dimensionalized by the initial vorticity thickness δ_0, the low-speed velocity U_1 and density ρ. The convective velocity U_c is approximated by the average velocity of two sides $U_c = (U_1 + U_2)/2$. The corresponding Reynolds number reads $Re = U_c \delta_0 \rho / \mu$ where μ denotes the dynamic viscosity of the fluid. In this study, $Re = 200$ which defines a nearly inviscid dynamics.

Figure 1 illustrates the rectangular computational domain Ω, $x \in [-5, 75]$, $y \in [-15, 15]$ discretized on a unstructured grid with 10237 nodes. The inlet profile is a classical tanh profile

$$u = 2 + \tanh\left(\frac{2y}{\delta_0}\right), \quad v = 0, \quad \text{where} \quad \delta_0 = 1. \tag{2.1}$$

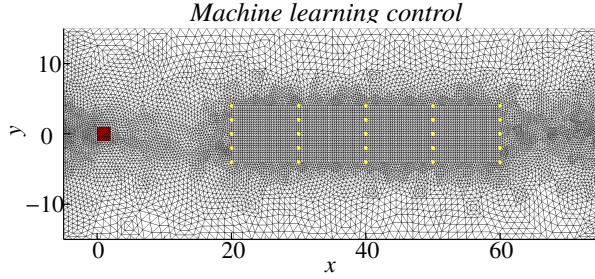The inlet velocity profile is perturbed by a small stochastic excitation of u component in the center

Figure 1: The computational domain. 25 sensors (yellow dots) are located at grid nodes to monitor the instantaneous velocity. The transverse volume force as actuation is added in an upstream zone (red shade).

at $y \in [-2, 2]$ with a standard deviation of $0.01U_c$. This perturbation accelerates the evolution of the Kelvin-Helmholtz vortices.

A direct numerical simulation of the incompressible mixing layer is performed by an in-house solver based on the finite element method. The numerical integration is second-order accurate in space and fully implicit third-order accurate in time. The details can be referred to Ishar *et al.* (2019).

The flow is manipulated by an upstream transverse unit volume force in the small domain $(x, y) \in [0, 2] \times [-1, 1]$ (see the red shade in figure 1). The volume force is driven by the actuation command b. The absolute value of the command is limited by unity to mimick experimental limits on actuation authority. The flow is monitored by an array of $N_s = 25$ sensors for the streamwise velocity component. The sensors (yellow dots in figure 1) are distributed in a rectangular area with $x \in \{20, 30, 40, 50, 60\}$ and $y \in \{0, \pm2, \pm4\}$. The computational mesh has been adjusted for an accurate placement of the sensors on the nodes. The feedback signal $s(t)$ comprises all velocity components of these sensors.

The goal of sensor-based control is to minimize or maximize the cumulative fluctuation energy of the sensors. The signal fluctuation $s_i' = s_i(t) - \langle s_i(t)\rangle_\tau$ is obtained based on the moving average $\langle s_i(t)\rangle_\tau = (1/\tau) \int_{t-\tau}^t s_i(t)$ over $[t - \tau, t]$ with a time window $\tau = 2/f$, where $f = 0.1075$ is the dominant frequency of the natural mixing layer. The averaged cumulative fluctuation energy reads

$$K = \sum_{i=1}^{N_s} \left\langle s_i'^2(t)\right\rangle_T . \tag{2.2}$$

Here, the averaging window is $T = 320$ corresponding to 8 downwash times ($80/U_c = 40$) through the whole compuational domain. For control purposes, the sensor-based control law shall maximize (minimize) the kinetic energy K, to destabilize (stabilize) the mixing layer. We define the cost function as $J_d = 1/K$ ($J_s = K$) for destabilizing (stabilizing) the mixing layer.

3. Machine learning control augmented with data analysis

Machine learning control (MLC) (Ren *et al.* 2020) has been applied to numerous experimental and numerical plants. MLC can self-learn nonlinear multiple-input multiple-output feedback laws minimizing a cost function using powerful methods of machine learning, like reinforcement learning, genetic algorithms and genetic programming. Here, we focus on linear genetic programming control (LGPC), which has discovered the arguably most complex multiple-input multiple-output laws for distributed actuation of a turbulent jet (Zhou *et al.* 2020). Often hundred to thousand control laws are tested before convergence. This data can provide valuable insight into the complexity of the control problem and the associated flow physics. In this section, we propose
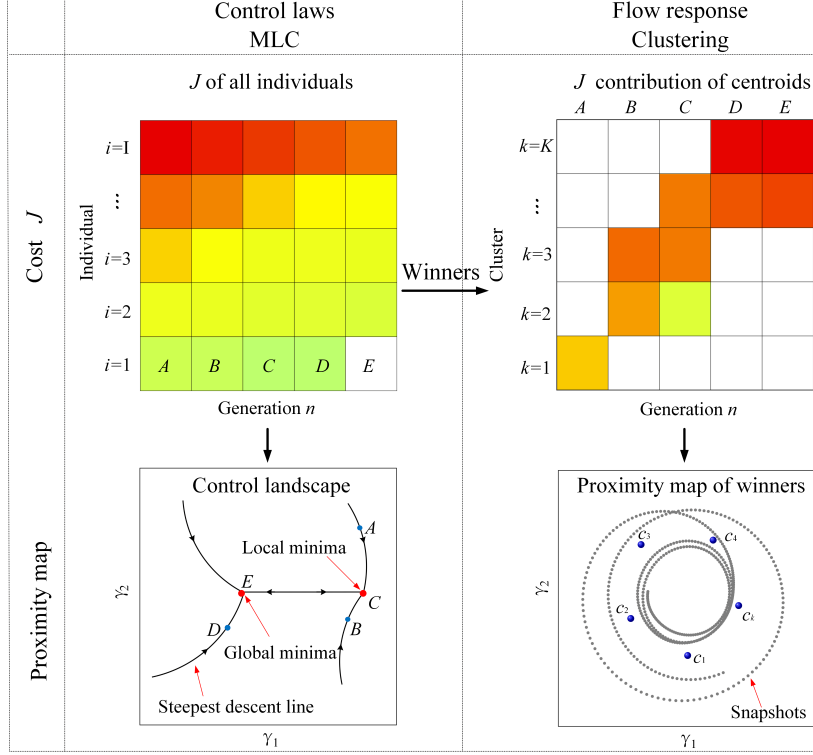
Figure 2: Principle sketch for augmented machine learning control. For details see text.

an analysis methodology for this data. The goal is to identify qualitatively different actuation mechanisms and their corresponding coherent structure dynamics.

Following Li *et al.* (2018), the control law is searched in the large space comprising sensor feedback and multi-frequency forcing and combinations thereof. This space includes many known stabilizing and destabilizing mechanisms, like phasor control or low- and high-frequency actuation. The ansatz for the control law reads

$$b = K(\boldsymbol{s}'(t), \boldsymbol{h}(t)). \tag{3.1}$$

Here, $\boldsymbol{s}'$ comprises N_s sensor fluctuations introduced in § 2. And $\boldsymbol{h}$ includes harmonic signals at natural frequency f, half and twice that frequency,

$$\boldsymbol{h}(t) = \begin{bmatrix} \cos(2\pi f t) & \cos(\pi f t) & \sin(\pi f t) & \cos(0.5\pi f t) & \sin(0.5\pi f t) \end{bmatrix}^{\dagger} \tag{3.2}$$

The harmonics include sines and cosines for the construction of phase differences. These phase differences may have significant effect on mixing layers (Coats 1997). Without loss of generality, $\sin 2\pi f t$ is omitted as only phase differences between different frequencies are of dynamic importance and a phase in the first harmonics can be removed by a time shift.

The optimization of (3.1) with respect to the cost J is performed with LGPC with typical parameters (Li *et al.* 2018) (see Appendix A). The population size is $N_i = 100$ and convergence is reached after N_g generations. LGPC leads to $N = N_i \times N_g$ control laws K_i^n with cost J_i^n, where i and n are the indices of the individual and generation, respectively. The simulation of each control law leads to $N_t = 800$ equidistantly sampled flow snapshots resolving the post-transient behaviour with time step 0.1 representing two downwash times.

In the following, this data base is harvested for physical insights (see figure 2). Starting point

is a completed MLC with N_g generations of N_i individuals (top left of figure 2). First, the tested ensemble of control laws are visualized in a control landscape (bottom left of figure 2). In the following, i denotes the dummy index over all N control laws K_i and costs J_i. Following Li *et al.* (2018), the distance between two control laws K_i and K_j is quantified by

$$D_{ij} = M_{ij} + \alpha \left| J_i - J_j \right| \tag{3.3}$$

where $M_{ij} = \langle |K_i - K_j|^2 \rangle_{i,j}$ is the time-averaged difference of the actuation commands and the second term penalizes performance differences. The penalization parameter α is chosen so that the maximum difference between control laws M_{ij} equals the maximum difference $\alpha |J_i - J_j|$. Thus, the symmetric configuration matrix $\boldsymbol{D} = (D_{ij})$ is based on control laws and cost functions.

The similarity and performance of the control laws is visualized in a two-dimensional control landscape, where each control law K_i has an associated feature vector $\boldsymbol{\gamma}_i = \left[\gamma_{i,1}, \gamma_{i,2} \right]^\dagger$. The distance between the feature vectors optimally approximates D_{ij}, i.e., $\|\boldsymbol{\gamma}_i - \boldsymbol{\gamma}_j\|^2 \approx D_{ij}^2$. Thus neighbouring (distant) feature vectors represent similar (dissimilar) control laws or performances. This goal is achieved with classical multidimensional scaling (CMDS) (Cox & Cox 2000).

As novel feature, the topology of the control landscape $J(\boldsymbol{\gamma})$ is illustrated with 'steepest descent' lines which terminate in local or global minima. Starting from $\boldsymbol{\gamma}_i$, the closest 15 neighbours are determined, corresponding to 2% of the control laws. Now, $\boldsymbol{\gamma}_i$ is connected to $\boldsymbol{\gamma}_j$ which has the lowest value of these neighbours. The steepest descent continues from $\boldsymbol{\gamma}_j$ analogously until the trajectory terminates in a minimum. These steepest descent trajectories are determined for every feature vector. The line width of a line from i to j increases with the number of passages from all trajectories. Thus, deep valleys will be marked by thick lines.

The learning process of MLC with increasing generations is illustrated by a comparison of the snapshots of the best individuals, also called 'winners' in the following. The winner snapshots $\boldsymbol{u}^m$, $m = 1, \ldots, M$ are coarse-grained into few representative centroids $\boldsymbol{c}_k$, $k = 1, \ldots, K$ by a k-means++ algorithm (see Appendix B). Each snapshot can be associated with its closest centroid. Thus, snapshots are 'binned' into clusters. This coarse-graining allows to visualize and inspect all centroids and potentially give them a physical meaning (top right of figure 2).

The total fluctuation level is exactly given by $J_i = \sum_{k=1}^{K} p_{i,k} J_{i,k}$, where $p_{i,k}$ is the population of a cluster k by the ith control law, and $J_{i,k}$ corresponds to the fluctuation level associated with that cluster k. Now, beneficial and less beneficial clusters are indicated by the local cost function $J_{i,k}$. The machine learning process of a control law should increasingly populate increasingly better centroids while avoiding worse centroids, as observed by Nair *et al.* (2019).

The neighbourhood relation between snapshots and centroids are visualized with another CMDS-based proximity map (bottom right of figure 2). Thus, the temporal evolution of the Navier-Stokes simulatons can be mapped as trajectories in a two-dimensional plane with the centroids as 'light houses'. Cluster-based network modeling (Li *et al.* 2020) provides an automated path to dynamic reduced-order models. The potential of this framework will become apparent in the result section and will be critically discussed in the conclusions.

4. Feedback control of the mixing layer

First, linear genetic programming control (LGPC) is applied to stabilize and destabilize the mixing layer with the ansatz (3.1). A priori, the optimal strategy is far from being clear. Open-loop low-frequency forcing may excite vortex pairing and thus destabilize the mixing layer. Open-loop high-frequency forcing is reported to stabilize the flow. Feedback mechanisms may or may not be better than periodic or multi-frequency forcing. The mixing layer is notoriously difficult to stabilize with a continuum of unstable frequencies.

Figure 3 presents the MLC results for minimizing and maximizing the fluctuation energy (2.2)

(a)
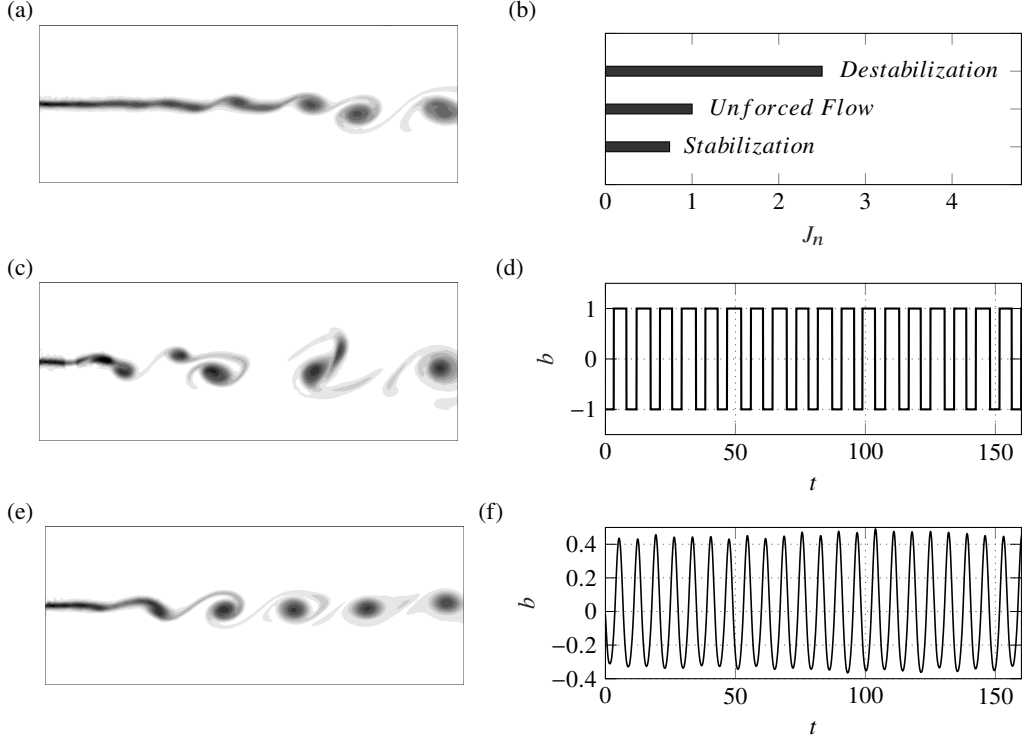
(b)

(c)

(d)

(e)

(f)

Figure 3: Machine learning control results for destabilizing and stabilizing the mixing layer. (a) The spanwise vorticity of the natural regime. (b) The performance of the linear genetic programming control. (c) and (e) respectively display the instantaneous spanwise vorticity of destabilizing and stabilizing the mixing layer with the best control law displayed in (d) and (f).

after 6 generations with 100 individuals. The unforced benchmark (subfigure a) shows Kelvin-Helmholtz vortices which tend to pair at the end of the domain. For destabilization, MLC achieves the increase of fluctuation energy by a factor 2.5 (see subfigure b) with the excitation of early multiple vortex pairings (see subfigure c). MLC converges to a sensor-based feedback control and ignores the harmonic frequency input,

$$b = -e^{s'_4}/s'_{21}. \tag{4.1}$$

From subfigure d, the actuation command is nearly periodic 'bang-bang' type, i.e., assumes the maximum amplitude permitted by the constraint $|b| \leqslant 1$. The frequency is about half of the natural Kelvin-Helmholtz value. The exponential factor remains positive. Hence, effectively, the control only listens to the sign of s'_{21} at the bottom left corner $x = 20$, $y = -4$ of the sensor probes. The feedback destabilization is similar to an MLC experiment with upstream jets and a downstream hot-wire rake (Li *et al.* 2018).

Stabilization of the mixing layer is a much harder task. LGPC achieves a 26% reduction of the fluctuation level (see figure 3b). Intriguingly, the control mechanism is not a delay of vortex formation but early excitation of pure higher-frequency Kelvin-Helmholtz vortices which neither grow nor not pair (see figure 3e). Again, the best control law is of pure sensor feedback type,

$$b = 0.075182 - s'_7 \times \cos(s'_{22}). \tag{4.2}$$

The actuation command induces a net upward force and feeds back s'_7, a sensor signal at $x = 40$
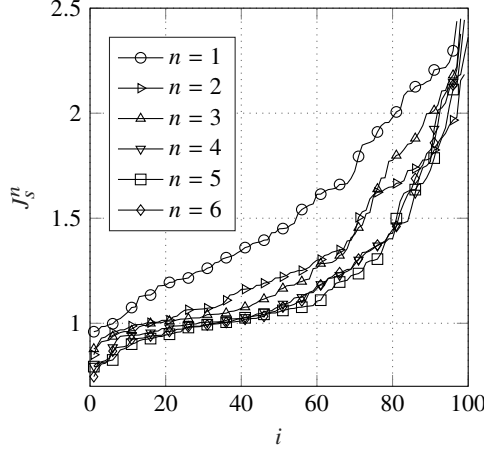
Figure 4: Mixing layer stabilization: Evolution of the normalized cost J_i^n for the individuals $i = 1, \ldots, 100$ and generations $n = 1, \ldots, 6$. For clarity, every fifth individual is displayed.
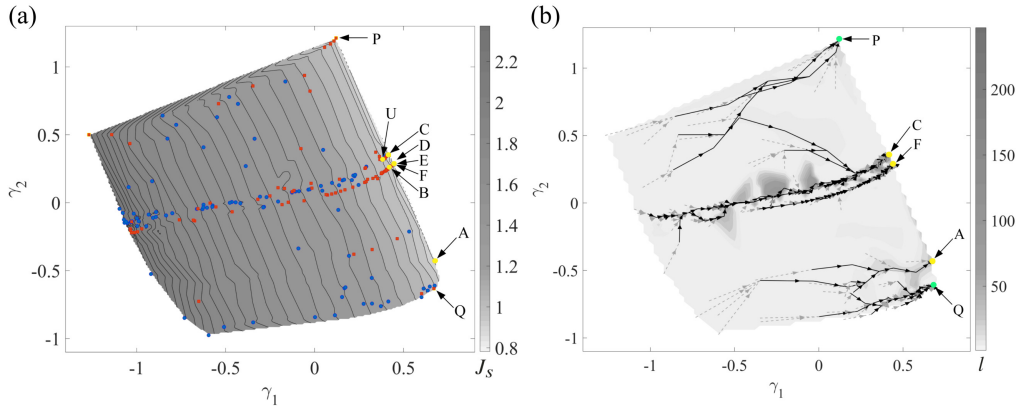

Figure 5: The evolution of machine learning control for stabilizing the mixing layer. (a) Control landscape for $n = 6$ generations. (b) Ridgeline topology of the control landscape via steepest descent lines. For details see text.

and $y = 2$. The cosine factor is a small modulation from s'_{22} at the same downstream location $x = 40$ but on the other side $y = -2$ of the mixing layer.

The learning curve of mixing layer stabilization (figure 4) reveals the difficulty of the control task: Nearly all individuals of the initial generation $n = 1$ are worse than no forcing at all and few individuals of the subsequent generations beat the unforced benchmark of unity. The learning process is stopped at sixth generation.

In the following, we explore the data base generated by stabilizing LGPC with $100 \times 6 = 600$ simulations. Figure 5a shows the control landscape discussed in § 3. The individuals of the first generation (blue dots) span large portion of the landscape. The individuals in the sixth generation (red dots) assemble on the right side with increasing γ_1. The winners of the $n = 1, \ldots, 6$ are denoted by yellow circles marked A to F, respectively. The interpolated cost values are color-coded according to the legend. Increasing γ_1 clearly reveals a better behavior of stabilizing mixing layer. The stabilization challenge may be appreciated by the closeness of the best individuals B to F of generation $n = 2, \ldots, 6$ to the unforced flow marked by U.
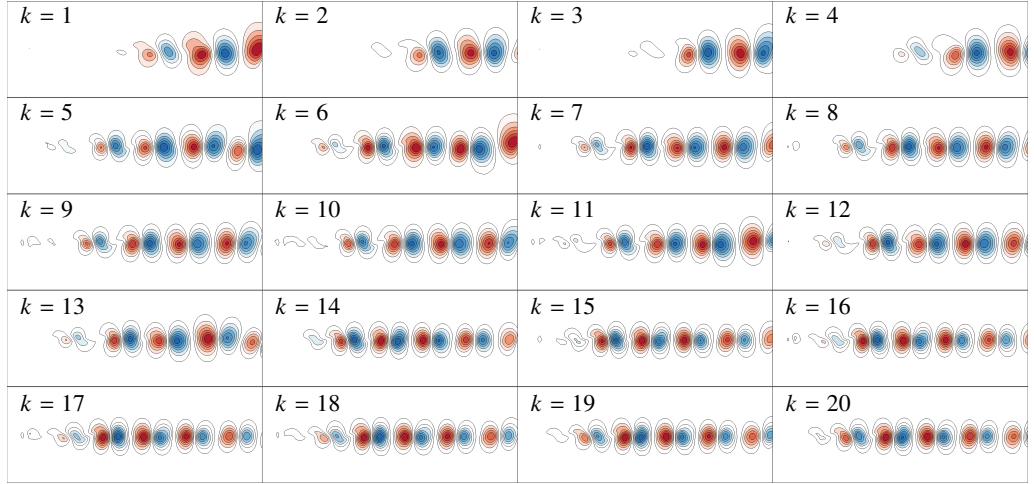
Figure 6: The $k = 20$ centroids of the natural flow and winners in each generation.
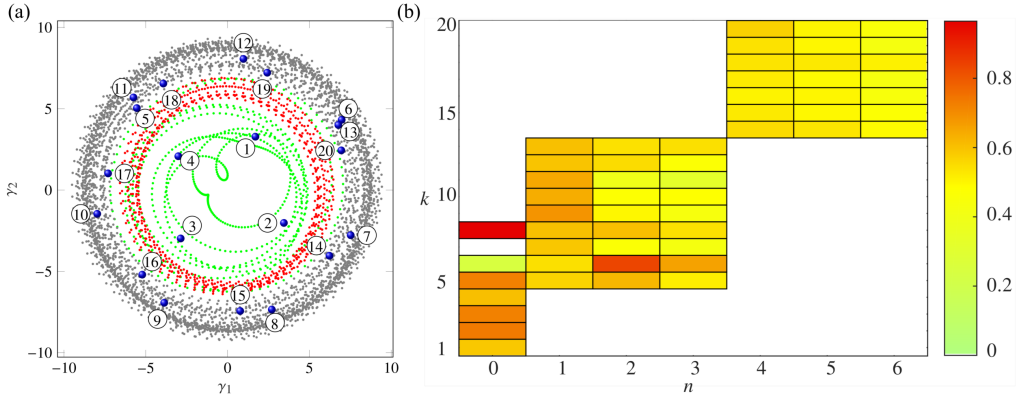

Figure 7: (a) Proximity map of the winners for stabilizing mixing layer simulations showing the centroids (blue balls) and snapshots (dots). The green dots represent the snapshots of unforced attractor while the red dots denote the snapshots from the attractor of best control law. Other gray dots represent the winner snapshots of generation 2 to 5. (b) Fluctuation level of the clusters corresponding to the winners of each generation. M denotes the index of generation.

In figure 5a, the control landscape is not populated evenly. The individuals seem to populate lines as also observed in many other MLC studies. The steepest descent lines (see figure 5b), discussed in § 3, seem to offer an explanation. Line segments which are shared by at least 20 of the search pathways are highlighted as black solid arrows and considered as the important pathway. The control landscape has 5 local minima marked by red circles on the right side associated with the winners A, C, F and two suboptimal individuals Q and P from the last generation. The steepest descent lines seem to quickly converge to 5 valleys leading to these 5 minima. The valley may be a true ridgeline or a manifold which becomes one-dimensional after projection. A closer investigation of higher feature coordinates γ_i, $i \geqslant 3$ may yield additional insight. Summarizing, this analysis provides strong indication that stabilization is difficult, was not achieved in the first Monte-Carlo generation and is associated with multiple minima.

The control landscape may provide important insights of dynamic domains with different behaviour. In the following investigation, an understanding of the actuated coherent structure

dynamics shall be achieved from the unforced flow refereed to as $n = 0$ and the winners of generations $n = 1, \ldots, 6$. For every control law 800 subsequent snapshots are investigated corresponding to two downwash times. An exhaustive visualization and conclusive interpretation of all snapshots is typically beyond the scope of possibilities. Here, we offer an automated coarse-graining into $K = 20$ centroids, These centroids are conveniently visualized in figure 6. The similarity of the snapshots and centroids is indicated in a 2D proximity map (figure 7a). The motion between centroids reveal the state transitions during the evolution of machine learning control. The inner green dots denote the unforced flow populated cluster $k = 1$ to 4 featuring long wavelength vortices and at cluster $k = 5, 6, 7$ featuring short wavelength K-H vortices while 8 describes the vortex shedding of the unforced flow. The winners of generation from $n = 1$ to 3 are described by the cluster from $k = 5$ to 14. The flow field of the winners are gradually tamed into a uniform limit cycle dynamics exhibiting K-H structures corresponding to the high-frequency forcing ($k = 15$ to 20).

Figure 7b sheds light on the MLC optimization process and progressive migration from suboptimal to more optimal flow states. The abscissa marks the considered winners $n = 0, \ldots, 6$ while colored boxes indicate the populated centroids $k = 1, \ldots, 20$. The fluctuation contribution K_k of each centroid is given by (4.3)

$$K_k = \frac{\sum_{m=1}^{M} \chi_k^m \sum_{i=1}^{N_s} s_i'^2(t)}{\sum_{m=1}^{M} \chi_k^m}. \tag{4.3}$$

Here, χ_k^m is unity if the snapshot m belongs to cluster k and vanishes otherwise. The sum of these centroidal cost values K_k weighted by the population p_k is exactly the total fluctuation level $K = \sum_{k=1}^{K} p_k K_k$. The color code of figure 7b indicates the K_k value of every centroid. As expected, increasing performance is related to lower K_k values. Note that one centroid may have slightly different K_k values for different control laws $n = 0, \ldots, 6$, because the mean flow is different.

5. Conclusions

We have augmented machine learning control (MLC) by an automated analysis of the control law and associated flow data. The analysis comprises (1) a control landscape with indications of local minima and ridgelines, (2) a coarse-graining of snapshots from the best performing control laws into a small number of centroids, (3) an analysis of coherent structures represented by the centroids and the associated cost and (4) a proximity map of the flow states visualizing the dynamics. The augmented MLC has been successfully applied to the stabilization of the mixing layer. The control landscape indicated multiple local minima connected to rigdelines in long valleys. The learning process of MLC reveals increasingly more efficient coherent structures. A feedback law replaces unforced Kelvin-Helmholtz vortices with subsequent vortex pairing by pure higher-frequency vortices which do not grow in streamwise direction. Thus, a reduction of the fluctuation energy by 26 % was achieved. In contrast, mixing layer destablization with MLC achieved an increase of the fluctuation energy by a factor 2.5 by maximum amplitude feedback excitation of early multiple vortex pairing.

We see the proposed analysis as a start to a comprehensive machine learning control and modeling strategy, where self-learning of increasingly better control laws provide the data base for (1) an automated classification of qualitatively different dynamic regimes, (2) an automated distillation of the most relevant coherent flow structures, and (3) automated development of a control-oriented reduced-order model approximating the full plant for a large range of control laws. The control landscape and clustering are the starting point for tasks (1) and (2). Preliminary

Parameters	Values
Population size	$N_i = 100$
Tournament size	$N_T = 7$
Elitism size	$N_e = 1$
Replication probability	$P_r = 10\%$
Crossover probability	$P_c = 60\%$
Mutation probability	$P_m = 30\%$
Operators	$+, -, x, \div, \sin, \cos, \tanh, \exp, \log$
Minimal instruction number	5
Maximal instruction number	25
Number of constants	$N_c = 6$
Constant range	$[-1, 1]$

Table 1: LGPC parameters

results on cluster-based network models (Li *et al.* 2020) make them a likely candidate for task (3). The automation of these tasks liberates time for deep first-principle based physics investigations.

Acknowledgements

Declaration of interests

The authors report no conflict of interest.

Appendix A. Linear genetic programming control

In the present study, the control goal for the mixing layer is to minimize (stabilization) or maximize (destabilization) the cumulative fluctuation energy K of the sensors (see eq. (2.2)). Following Li *et al.* (2017); Zhou *et al.* (2020), the control design is formulated as a regression problem: Find the best control law mapping the plant output to plant input which minimizes the cost function. We have defined the cost function as $J_d = 1/K$ ($J_s = K$) for destabilizing (stabilizing) the mixing layer. The regression problem is solved by linear genetic programming (LGP) which can be referred to Brameier & Banzhaf (2007). Duriez *et al.* (2017) successfully employed the genetic programming (GP) algorithm to mitigate flow separation and promote mixing. LGP is a variant of GP and capable of finding simple, powerful and general regression method for control laws of closed-loop control framework. We refer to this method as linear genetic programming control (LGPC).

The control law is formulated as a sequence of instructions operating on a set of sensors s and harmonic functions h, operators $(+, -, x, \div, \sin,...)$ and constants. Table 1 lists the LGPC parameters for this study. LGPC initializes with the first generation containing N_i individuals (i.e., control laws) randomly like in a Monte Carlo method. Each control law will be evaluated in the numerical simulation plant and their performances on mixing layer destabilization and stabilization are quantified by the corresponding cost values J. The next generation is evolved

by elitism and genetic operations. The elitism is an operation which directly copy N_e individuals of n th generation with top ranking cost values to the $(n + 1)$th generation. This ensures the new generations won't perform worse than the previous ones. The remaining $(N - N_s)$ individuals of $(n + 1)$th generation will be generated by three genetic operations including crossover, mutation and replication with specific selection probabilities. The selected individual(s) for these three operations are the winner(s) of a tournament process. N_T randomly selected individuals of nth generation enter into a tournament process and the winner is determined by its cost value J. Crossover randomly exchanges substructures of two individuals, which is beneficial to breeding better potential individuals among well-performing individuals. Mutation randomly changes a substructure in an individual. This operation might explore new local minima. Replication copies an individual to next generation without any change. This results in a memory of the past generation. These three genetic operators are stochastic in nature and have a fixed selection probabilities. We set the probabilities for three genetic operations $P_r = 10\%$, $P_c = 60\%$ and $P_m = 30\%$ which are classical and result in good results in previous studies (Li *et al.* 2017; Wu *et al.* 2018; Zhou *et al.* 2020). The procedure is iterated until some stopping criterion is reached, e.g., LGPC cannot find an individual with a much lower cost value J.

To get a fast convergence for LGPC, a pre-selection of individuals is designed for all generations. Each individual is pre-evaluated based on the velocity fluctuation s' from $N_s = 25$ sensors of natural flow. An individual will be excluded if its actuation command b is a constant during more than half time period, or a replicate of previous individuals. A new individual will be generated to replace the bad performer in the pre-evaluation step.

Appendix B. Clustering as coarse-graining

Cluster analysis lumps similar objects into bins, called 'clusters'. This lumping of data is performed in an unsupervised manner, i.e., no advance labeling or grouping of the data has been performed. We consider a sequence of velocity field snapshots denoted $\boldsymbol{u}^m(\boldsymbol{x}) := \boldsymbol{u}(\boldsymbol{x}, t^m)$, $m = 1, \ldots, M$ in a steady domain Ω from experiments or numerical simulations. The velocity field is equidistantly sampled with time step Δt, i.e. the mth instant reads $t^m = m\Delta t$. These velocity snapshots are coarse-grained into K clusters in terms of their similarities. The representative states of each cluster is characterized by centroids $\boldsymbol{c}_k$. The similarity of any two velocity fields $\boldsymbol{u}^m, \boldsymbol{u}^n$ is measured using Euclidean distance D, i.e.,

$$D(\boldsymbol{u}^m, \boldsymbol{u}^n) = \sqrt{\int_\Omega \mathrm{d}x \|\boldsymbol{u}^m - \boldsymbol{u}^n\|^2}. \tag{B 1}$$

The distance is calculated based on the norm associated with the Hilbert space $\mathcal{L}^2(\Omega)$ of square-integrable functions. The whole computational domain Ω is employed for the integration.

A set of K centroids $\boldsymbol{c}_k$ are randomly initialized and their performances are evaluated by the total inner-cluster variance V of snapshots $\boldsymbol{u}^m$ with regard to the nearest centroid $\boldsymbol{c}_k$,

$$V(\boldsymbol{c}_1, \ldots, \boldsymbol{c}_k) = \sum_{k=1}^K \sum_{\boldsymbol{u}^m \in C_k} D(\boldsymbol{u}^m, \boldsymbol{c}_k). \tag{B 2}$$

Finally, a set of optimal centroids $\boldsymbol{c}_k^{opt} (k = 1, \ldots, K)$ are determined to minimize the inner-cluster variance V in (B 2).

$$(\boldsymbol{c}_1^{opt}, \ldots, \boldsymbol{c}_K^{opt}) = \underset{\boldsymbol{c}_1, \ldots, \boldsymbol{c}_K}{\arg \min} V(\boldsymbol{c}_1, \ldots, \boldsymbol{c}_K) \tag{B 3}$$

This optimization problem is solved using the iterative k-means algorithm (MacQueen 1967; Lloyd 1982). The iteration will stop until the convergence is reached or while the variance V is

small enough. As no convergence to a global minimum can be guaranteed, k-means++ performs 1000 k-means iterations with different initial conditions and takes the best result.

The centroids characterize the typical flow patterns of each clusters, also called modes in the ROM community. The corresponding cluster-affiliation function maps a velocity field $\boldsymbol{u}$ to the index of the closest centroid,

$$k(\boldsymbol{u}) = \arg\min_i \|\boldsymbol{u} - \boldsymbol{c}_i\|_\Omega, \tag{B 4}$$

This function defines cluster regions as Voronoi cells around the centroids

$$C_i = \left\{ \boldsymbol{u} \in \mathcal{L}^2(\Omega) \colon k(\boldsymbol{u}) = i \right\}. \tag{B 5}$$

This function can also be employed to map a snapshot index m to the representative cluster index $k(m) := k\left(\boldsymbol{u}^m\right)$. Alternatively, the characteristic function

$$\chi_i^m := \begin{cases} 1, & \text{if} \quad i = k(m) \\ 0, & \text{otherwise} \end{cases} \tag{B 6}$$

describes if the mth snapshot is affiliated with the lth centroid. The latter two quantities are equivalent.

The number of snapshots n_k in cluster k is given by

$$n_k = \sum_{m=1}^M \chi_k^m \tag{B 7}$$

The centroids are the mean velocity field of all snapshots in the corresponding cluster. In other words,

$$\boldsymbol{c}_k = \frac{1}{n_k} \sum_{\boldsymbol{u}^m \in C_k} \boldsymbol{u}^m = \frac{1}{n_k} \sum_{m=1}^M \chi_k^m \boldsymbol{u}^m. \tag{B 8}$$

In the centroid visualizations (figure 6) , we accentuate the vortical structures by displaying the fluctuations $\boldsymbol{c}_k - \overline{\boldsymbol{u}}$ around the snapshot mean $\overline{\boldsymbol{u}}$ and not the full velocity field $\boldsymbol{c}_k$.

In this study, we conduct the cluster analysis with post-transient snapshots from the natural flow and the 6 winners of generations. From each of these 7 flows, also called attractors in the sequel, 800 snapshots with sampling frequency of 10 are taken. Note that $n = 0, \ldots, 6$ is the index of the control law (attractor) and $N_t = 800$ is the number of the snapshots for each law. All this 5600 snapshots are used for clustering.

Let $N_{i,k}$ be the number of snapshots of the ith attractor data in the kth data. Let $N_i = \sum_{k=1}^K N_{i,k}$ be the total number of snapshots of the ith attractor data. The probability that a snapshot belonging to the ith operating condition lies in the k th cluster is estimated by

$$p_{i,k} = \frac{N_{i,k}}{N_i} \tag{B 9}$$

The probability describes the relative frequencies of cluster visits.

REFERENCES

BENARD, N., PONS-PRATS, J., PERIAUX, J., BUGEDA, G., BRAUD, P., BONNET, J.P. & MOREAU, E. 2016 Turbulent separated shear flow control by surface plasma actuator: experimental optimization by genetic algorithm approach. *Exp. Fluids* **57** (2), 22:1–17.

BRAMEIER, MARKUS F & BANZHAF, WOLFGANG 2007 *Linear genetic programming*. Springer Science & Business Media.

BRUNTON, S. L. & NOACK, B. R. 2015 Closed-loop turbulence control: Progress and challenges. *Appl. Mech. Rev.* **67** (5), 050801:01–48.

COATS, C.M. 1997 Coherent structures in combustion. *Prog. Energy Combust. Sci* **22**, 427–509.

COX, T. F. & COX, M. A. A. 2000 *Multidimensional Scaling*, 2nd edn., *Monographs on Statistics and Applied Probability*, vol. 88. Chapman and Hall.

DURIEZ, T., BRUNTON, S. L. & NOACK, B. R. 2017 *Machine Learning Control-Taming Nonlinear Dynamics and Turbulence*. Springer.

FUKAMI, K., FUKAGATA, K. & TAIRA, K. 2020 Assessment of supervised machine learning methods for fluid flows. *Theor. Computat. Fluid Dyn.* **34**, 497–519.

ISHAR, R., KAISER, E., MORZYNSKI, M., ALBERS, M., MEYSONNAT, P., SCHRÖDER, W. & NOACK, B. R. 2019 Metric for attractor overlap. *J. Fluid Mech.* **874**, 720–752.

KOUMOUTSAKOS, P., FREUND, J. & PAREKH, D. 2001 Evolution strategies for automatic optimization of jet mixing. *AIAA J.* **39** (5), 967–969.

LI, H., FERNEX, D., TAN, J., MORZYŃSKI, M. & NOACK, B. R. 2020 Cluster-based network model of an incompressible mixing layer. *J. Fluid Mech.* **submitted, http://arxiv.org/abs/2001.02911**.

LI, R., NOACK, BERND R., CORDIER, LAURENT, BORÉE, JACQUES & HARAMBAT, FABIEN 2017 Drag reduction of a car model by linear genetic programming control. *Exp. Fluids* **58** (8), 103.

LI, R., NOACK, B. R., CORDIER, L., BORÉE, J., KAISER, E. & HARAMBAT, F. 2018 Linear genetic programming control for strongly nonlinear dynamics with frequency crosstalk. *Arch. Mech.* **70** (6), 505–534.

LLOYD, S. 1982 Least squares quantization in PCM. *IEEE Trans. Inform. Theory* **28** (2), 129–137.

MACQUEEN, J. 1967 Some methods for classification and analysis of multivariate observations. *Proc. of the Fifth Berkeley Symp. On Math. Stat. and Prob.* **1**, 281–297.

NAIR, A., YEH, C.-A., KAISER, E., NOACK, B. R., BRUNTON, S. L. & TIARA, K. 2019 Cluster-based feedback control of turbulent post-stall separated flows. *J. Fluid Mech.* **875**, 345–375.

PAREZANOVIĆ, V., CORDIER, L., SPOHN, A., DURIEZ, T., NOACK, B. R., BONNET, J.-P., SEGOND, M., ABEL, M. & BRUNTON, S. L. 2016 Frequency selection by feedback control in a turbulent shear flow. *J. Fluid Mech.* **797**, 247–283.

PASTOOR, M., HENNING, L., NOACK, B. R., KING, R. & TADMOR, G. 2008 Feedback shear layer control for bluff body drag reduction. *J. Fluid Mech.* **608**, 161–196.

RABAULT, J., KUCHTA, M., JENSEN, A., RÉGLADE, U. & CERARDI, N. 2019 Artificial neural networks trained through deep reinforcement learning discover control strategies for active flow control. *J. Fluid Mech.* **865**, 281–302.

REN, F., HU, H.-B. & TANG, H. 2020 Active flow control using machine learning: A brief review. *J. Hydrodyn.* **32** ((2)), 247–253.

WILTSE, J. M. & GLEZER, A. 2011 The effect of closed-loop feedback control on scalar mixing in a plane shear layer. *Exp. Fluids* **51**, 1291–1314.

WU, ZHI, FAN, DEWEI, ZHOU, YU, LI, RUIYING & NOACK, BERND R. 2018 Jet mixing optimization using machine learning control. *Exp. Fluids* **59** (8), 131.

ZHOU, Y., D., FAN, ZHANG, B., , LI, R. & NOACK, B. R. 2020 Artificial intelligence control of a turbulent jet. *J. Fluid Mech.* **897**, 1–46.